

# Self-compensating Light Calorimetry with Liquid Argon Time Projection Chamber for GeV Neutrino Physics

Xuyang Ning,<sup>1</sup> Wei Shi,<sup>2</sup> Chao Zhang,<sup>1,\*</sup> Ciro Riccio,<sup>2</sup> and Jay Hyun Jo<sup>1</sup>

<sup>1</sup>*Brookhaven National Laboratory, Upton, NY, 11973, USA*

<sup>2</sup>*Stony Brook University, SUNY, Stony Brook, New York 11794, USA*

(Dated: October 8, 2024)

Liquid Argon Time Projection Chamber (LArTPC) is an exceptional dual calorimeter capable of estimating the energy of incident particles through both the ionization charge and the scintillation light. Our studies show that due to the mechanisms of charge recombination and light generation involved in the energy dissipation in liquid argon, light calorimetry in LArTPCs is inherently self-compensating: the missing energy in the hadronic component is compensated for by the extra recombination luminescence compared to the electromagnetic component. Good compensation of the electron-to-hadron response ratio ( $e/h$ ) around unity can be achieved across a broad range of drift electric fields from 0.2 to 1.8 kV/cm. This inherent self-compensation enhances the appeal of light calorimetry in LArTPCs, complementing the well-established charge calorimetry. Using GeV neutrinos as a case study, we show that light calorimetry can achieve an energy resolution comparable to the more sophisticated charge imaging calorimetry. The synergy between light and charge calorimetry offers a novel approach to evaluating and mitigating systematic uncertainties in energy measurements with LArTPCs.

## I. INTRODUCTION

Estimating the energy of incident particles is an essential task in high energy physics experiments to study the fundamental properties of particles. For example, in neutrino oscillation experiments, the oscillation probabilities are expressed as a function of distance over neutrino energy ( $L/E_\nu$ ). Therefore, accurately estimating the neutrino energy with minimum bias and high resolution is a goal of all neutrino detectors. Calorimetry is an important detection principle in particle physics to measure particle energy [1]. A particle loses its energy in the calorimeter primarily through electromagnetic or hadronic interactions. The energy deposited by the charged particles in the instrumented material of the calorimeter can be detected in measurable signals, such as charge, light, heat, and so on. These signals are then used to estimate the initial energy of the incident particles after calibration and correcting for the missing energy not measured in the calorimeter.

Liquid argon (LAr) was proposed for calorimetry in 1974 by Willis and Radeka [2] and since then has been used by many particle physics experiments [3], such as E706 [4], SLD [5], D0 [6], H1 [7], and most recently, ATLAS [8]. As a noble liquid detector, LAr produces large signals of both ionization charge and scintillation light when energy is deposited inside, although almost all previous collider LAr calorimeters are ionization chambers that only collect ionization electrons with short drift distances. Because of the relatively long radiation length of LAr and the size constraint in collider experiments, those LAr ionization chambers also consist of denser absorbers (e.g. copper or tungsten) to contain the energy

and act as sampling calorimeters. This LAr sampling calorimeter solution is cost-effective, provides good energy resolution, linearity, uniformity, fast response, and has negligible radiation damage. Therefore, it is particularly attractive to high energy (GeV to TeV) and high luminosity accelerator experiments.

The technology of using LAr as a scintillation calorimeter has been mainly driven by dark matter experiments, such as DEAP-3600 [9], WArP [10], DarkSide-50 [11], and DarkSide-20k [12]. Since dark matter experiments desire low energy thresholds (tens of keV) and the capability of distinguishing electronic recoils from nuclear recoils, much effort was invested in understanding the LAr scintillation mechanism, light yield, scintillation timing, response to energy transfer, optical transport properties, and so on. LAr scintillation calorimeter for few-hundred-MeV or higher particle energy measurement has not been fully studied or utilized so far compared to other noble liquid detectors such as LKr [13] or LXe [14], mainly because of its longer radiation length resulting larger sized detector needed.

In recent years, the technology to build massive and homogeneous liquid argon time projection chambers (LArTPCs) has advanced tremendously, owing to its many advantages in neutrino detection such as the cost-effectiveness, scalability, and high spatial resolution for particle identification. The concept was first proposed in the 1970s [15, 16] and the first large LArTPC detector, ICARUS T600 [17], operated in 2010. Many LArTPC experiments have been built since then, such as MicroBooNE [18], ICARUS [19], SBND [20], ProtoDUNE-SP [21]. and the upcoming Deep Underground Neutrino Experiment (DUNE) [22]. In the current-generation LArTPC neutrino experiments, the ionization charge signal is the main detection channel. With a uniform electric field applied in the TPC between the cathode and anode planes, the ionization electrons drift toward the

\* czhang@bnl.gov

anode at a constant speed. The drift time of the electron can be translated into its position along the drift direction. The transverse positions can be determined by the multiple wire planes, or printed circuit boards, at the anode where the parallel sense wires or strips are oriented at different angles. Pixelated electrodes at the anode have also been developed in recent years [23]. Together, a 3D image of the particle activities can be reconstructed with a millimeter-scale position resolution. Meanwhile, the energy deposition per unit length ( $dE/dx$ ), also called the linear energy transfer (LET), can be measured along the particle trajectories to provide further particle identification information. Since high purity can be achieved in LAr, electrons can drift a few meters without attenuation, making it possible to build a large, fully active LArTPC calorimeter for neutrino detection.

Scintillation light is used in LArTPC neutrino detectors primarily to provide the starting time ( $t_0$ ) of the drift since the ionization charge signal does not provide the  $t_0$  information by itself. Light calorimetry was not fully utilized or studied in previous LArTPC neutrino detectors primarily because of their low photon collection efficiency and large position non-uniformity. This situation may be improved in future LArTPC detectors. For instance, the proposed reference design of the DUNE Phase-II far detectors, namely, the Aluminum Profiles with Embedded X-Arapucas (APEX) design [24], aims to increase the optical surface coverage to about 60% by instrumenting the entire field cage walls with large area photon detectors. Preliminary simulations show that the average light yield of this design can reach about 180 photoelectrons per MeV, similar in performance to other organic liquid scintillator detectors used in neutrino experiments. Therefore, it is timely to revisit the LArTPC as a scintillation light calorimeter and study how well it compares and supplements the well-established ionization charge calorimetry in LArTPC.

This paper is organized as follows. Section II briefly reviews the energy dissipation mechanism in LAr. In Sec. III, the deposited energy and missing energy in LArTPC is estimated for GeV neutrinos as a case study using Monte Carlo simulations. Section IV studies in detail the self-compensation mechanism observed in the LArTPC light calorimetry. Sec. V compares the energy resolution achieved from light calorimetry with charge-based calorimetry in reconstructing neutrino energy. Finally, Sec. VI discusses the applications of light calorimetry in the current and future experiments.

## II. ENERGY DISSIPATION IN LIQUID ARGON

The fundamental properties of liquid argon as a particle radiation detector have been extensively studied since the 1970s. In this section, we briefly review the energy dissipation mechanisms in LAr to establish the groundwork for later sections. More details can be found in Refs. [25–27].

Energy deposition in LAr creates either excited argon atoms ( $\text{Ar}^*$ ) or electron-ion ( $e^- - \text{Ar}^+$ ) pairs. The ratio  $\alpha$  between the number of  $\text{Ar}^*$ ,  $N_{\text{ex}}$ , and the number of  $\text{Ar}^+$ ,  $N_i$ , is calculated and measured to be 0.21 [26]:

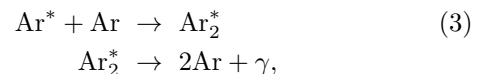
$$\alpha = \frac{N_{\text{ex}}}{N_i} = 0.21. \quad (1)$$

The energy required to produce one electron-ion pair in LAr is measured to be  $W_{\text{ion}} = 23.6$  eV [28]. If we treat the  $\text{Ar}^*$  and  $\text{Ar}^+$  equally as one quantized state, then it follows that the average energy, or a *quantum*, required to produce one state is:

$$W_{\text{ph}} = \frac{W_{\text{ion}}}{(1 + \alpha)} = \beta \cdot W_{\text{ion}} = 19.5 \text{ eV}, \quad (2)$$

where  $\beta = 1/(1 + \alpha) = 0.83$ .  $W_{\text{ph}}$  also corresponds to the energy needed to create one photon at zero electric field and will be elaborated later.

The ionization electrons in the electron-ion pairs can be collected under an external drift electric field and form the signals in charge calorimetry. The  $\text{Ar}^*$  will de-excite through the process [29]:

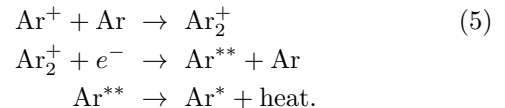


where a scintillation photon ( $\gamma$ ) is emitted in the process. The wavelength of the emission spectrum peaks at 127 nm, in the vacuum ultra-violet (VUV) region. The collection of these scintillation photons forms the signals in light calorimetry. The number of electrons ( $N_e$ ) and the number of scintillation photons ( $N_\gamma$ ) created by a certain energy deposition ( $E_{\text{dep}}$ ) in LAr can be calculated as:

$$\begin{aligned} N_e &= N_i = \beta \cdot \frac{E_{\text{dep}}}{W_{\text{ph}}}, \\ N_\gamma &= N_{\text{ex}} = (1 - \beta) \cdot \frac{E_{\text{dep}}}{W_{\text{ph}}}. \end{aligned} \quad (4)$$

For 1 MeV deposited energy, the total number of quanta created is  $\sim 51000$ , which consists of  $\sim 42000$  electrons and  $\sim 9000$  photons. This initial distribution of quanta is illustrated in Fig. 1.

The electrons and argon ions, however, go through another process called recombination during their passage in LAr [29]:



The resulting  $\text{Ar}^*$  goes through the same de-excitation process described in Eq. 3 and releases one scintillation photon. Therefore, the recombination process consumes the ionization electrons but creates more scintillation photons. The increase of scintillation light from recombination, also called recombination luminescence, was first

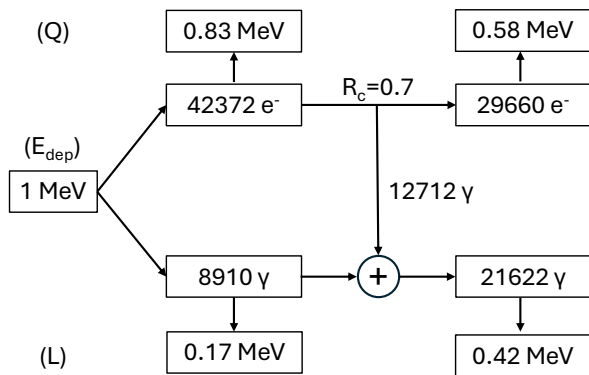


FIG. 1. Illustration of the distribution of quanta between electrons ( $e^-$ ) and scintillation photons ( $\gamma$ ) before and after charge recombination in LAr. The energy deposition ( $E_{\text{dep}}$ ) is assumed to be 1 MeV and the charge recombination factor is assumed to be  $R_c = 0.7$ . The number of quanta is converted into the visible energy in charge (Q) and light (L) assuming each quantum equaling 19.5 eV.

observed in 1977 [30]. This redistribution of quanta after recombination is also illustrated in Fig. 1. It is worth noting that the total number of quanta,  $N_e + N_\gamma$ , is conserved before and after the recombination process. The conservation of quanta has been observed experimentally at a range of  $dE/dx$  for various particles [29].

The mechanism of charge recombination in noble liquid has been studied in many literatures [31, 32]. The charge recombination factor  $R_c$ , defined as the ratio between the number of ionization electrons after recombination ( $N_e^r$ ) and before recombination ( $N_e$ ), is well described by the Birks model [31]:

$$R_c = \frac{N_e^r}{N_e} = 0.8 / \left( 1 + \frac{0.0486}{\mathcal{E}\rho} \cdot \frac{dE}{dx} \right), \quad (6)$$

where  $\mathcal{E}$  is the external electric field in kV/cm,  $\rho$  is the density of LAr in  $\text{g/cm}^3$ , and  $dE/dx$  is the energy loss per unit length in MeV/cm. For a minimum ionizing particle (MIP), the mean  $dE/dx$  in LAr is about 2.1 MeV/cm, and the recombination factor is about 0.7 at a typical 0.5 kV/cm electric field in LArTPC neutrino experiments.

At zero electric field, Eq 6 indicates that all ionization electrons will recombine, and an equal amount of scintillation photons will be generated. The ideal photon yield is therefore expected to be  $N_\gamma + N_e$ , i.e. about 51000 photons per MeV of deposited energy at zero electric field<sup>1</sup>. From this we can derive the light recombination factor  $R_L$ , defined as the ratio between the number of photons after recombination ( $N_\gamma^r$ ) and the ideal photon yield, to

be:

$$R_L = \frac{N_\gamma^r}{N_\gamma + N_e} = 1 - \beta R_c. \quad (7)$$

Figure 2 shows the charge and light recombination factors as a function of  $dE/dx$  in LArTPC, assuming a drift electric field of 0.5 kV/cm, where the  $dE/dx$  is normalized to that of a MIP. The recombination effect is the opposite between the charge and the light: The percentage of ionization electrons after recombination decreases for heavily ionizing particles compared with a MIP, while the percentage of scintillation photons increases. This forms the basis of the self-compensation mechanism in LArTPC light calorimetry, which will be further described in Sec. IV.

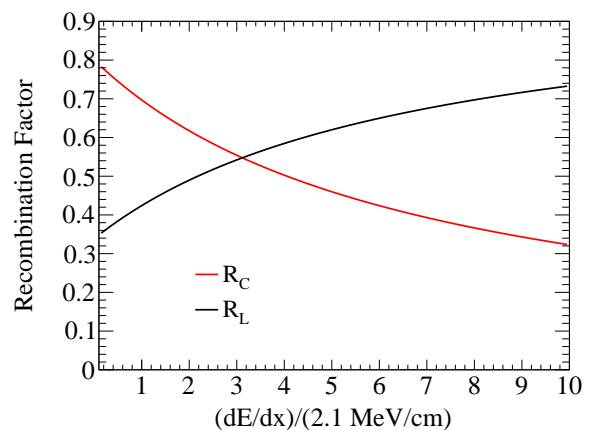


FIG. 2. The recombination factor for charge ( $R_c$ ) and light ( $R_L$ ) as a function of  $dE/dx$  in LArTPC based on Eq. 6 and 7. The external drift electric field is assumed to be 0.5 kV/cm. The  $dE/dx$  is normalized to that of a minimum ionizing particle, which is about 2.1 MeV/cm.

### III. ENERGY ESTIMATION IN LARTPC CALORIMETERS

The goal of the energy reconstruction is to estimate the initial energy of the incident particles from the observed signals in the calorimeter. A LArTPC can be considered as a dual calorimeter because both the charge and the light signals are recorded and can be used for energy estimation.

Energy reconstruction is typically performed in two steps. First, the energy deposited in the active material of the calorimeter is estimated from the observed signals in charge or light. Then, the initial energy of the incident particles is estimated by correcting for contribution from the invisible energy, or missing energy, which corresponds to the energy loss that does not create a signal in the calorimeter. Missing energy can originate from several mechanisms, such as energy loss in the inactive

<sup>1</sup> The effects to reduce the photon yield at zero E-field, as well as other quanta reducing processes, are discussed in Appendix B

materials, energy spent to break up the nuclei, escaping neutral particles such as neutrinos from particle decays, low-energy particles below the detection thresholds, and so on. Correcting missing energy generally requires a comprehensive detector Monte Carlo simulation study. In this section, we describe the methods involved in estimating the deposited energy and the missing energy in LArTPC.

### A. Deposited energy estimation

A LArTPC records charge and light signals as digitized waveforms. The charge sensors record induced electrical signals when ionization electrons pass by them. After dedicated signal processing and charge calibration [33], the signal waveforms can be converted to the number of ionization electrons detected, which is the same as  $N_e^r$  if we neglect the detection threshold. The light sensors record the photoelectron-induced signals when optical photons strike a sensor's photosensitive surfaces. Similarly, after signal processing and single photoelectron calibration, the signal waveforms can be converted to the number of photoelectrons ( $N_{pe}$ ) detected, which can be further converted into the total number of optical photons ( $N_\gamma^r$ ) given a calibrated photon collection efficiency (PCE).

There are different conventions to convert  $N_e^r$  and  $N_\gamma^r$  to the visible energy in charge ( $Q$ ) and light ( $L$ ), which only differ numerically before  $Q$  and  $L$  are further converted to the deposited energy  $E_{\text{dep}}$ . To take advantage of the conservation of quanta as explained in Sec. II, we recommend that each quantum, whether of an ionization electron or a scintillation photon, represents the same amount of energy. The most convenient choice of that energy is  $W_{\text{ph}}$ , or 19.5 eV. With this definition,  $Q$  and  $L$  become:

$$Q = W_{\text{ph}} \cdot N_e^r, \quad L = W_{\text{ph}} \cdot N_\gamma^r = \frac{W_{\text{ph}} \cdot N_{pe}}{\text{PCE}}. \quad (8)$$

Either  $Q$  or  $L$  can be used to estimate the deposited energy by correcting for the recombination effect described in Sec. II:

$$E_{\text{dep}} = \frac{Q}{\beta R_c} = \frac{L}{1 - \beta R_c}. \quad (9)$$

Since the charge recombination factor  $R_c$  is dependent on the  $dE/dx$  (cf. Eq. 6), without further corrections at the particle trajectory level, the  $E_{\text{dep}}$  estimation with an average  $R_c$  suffers from event-by-event fluctuations. The smearing of  $E_{\text{dep}}$  from charge recombination can be removed if we sum  $Q$  and  $L$  together:

$$\begin{aligned} Q + L &= W_{\text{ph}} \cdot (N_e^r + N_\gamma^r) \\ &= W_{\text{ph}} \cdot (N_e + N_\gamma) \\ &= E_{\text{dep}}. \end{aligned} \quad (10)$$

In this case, the conservation of quanta is transferred to the conservation of  $Q + L$ , and the  $E_{\text{dep}}$  estimation is

free of the recombination effect. Figure 1 illustrates the estimation of  $Q$  and  $L$  for a 1 MeV deposited energy with  $R_c = 0.7$ , and  $Q + L$  is conserved before and after recombination.

Eq. 9 and Eq. 10 show that there are three ways to estimate the  $E_{\text{dep}}$ : charge-only ( $Q$ ), light-only ( $L$ ), or charge-plus-light ( $Q + L$ ). It may appear that  $Q + L$ , being free of the recombination effect, is the best energy estimator. However, since the final goal is to reconstruct the initial energy of the incident particles, we have to consider the contribution from missing energy, which often is the dominant factor in energy resolution.

### B. Missing energy estimation

It is expected that some energy loss of the particles does not produce detectable signals and is, therefore, missing. Estimating this missing energy is essential in energy reconstruction and it is typically done through a detailed detector simulation using software packages such as Geant4 [34]. There are several contributors to the missing energy in general particle calorimeters:

*a. Inactive material* In sampling calorimeters, dense absorber materials are purposely placed in the detector to degrade the particle energy and contain the electromagnetic and hadronic showers. Absorber and active layers are typically alternately placed and only the active layers are instrumented to record the energy deposited inside. LArTPC, in contrast, can be built as a homogeneously active calorimeter. In this study, we consider an ideal, infinitely large LArTPC, and no inactive material is involved. In reality, a detector has a finite size and could consist of multiple modularized LArTPCs, so the energy loss in the structural materials, as well as the partially contained events, needs to be studied. It is also worth noting that the active volume for charge and light calorimetry could be different since scintillator light can be generated in the LAr region where there is no electric field, which is not considered in this study.

*b. Detection threshold* As particles slow down, their kinetic energy eventually becomes too small to generate a detectable signal. For charge calorimetry, the detection threshold of individual energy deposition depends on the electronic noise level. In most recent LArTPCs, such as MicroBooNE [35] and ProtoDUNE-SP [36], the equivalent noise charge (ENC) has achieved below 400  $e^-$  owing to the implementation of cryogenic electronics. In this study, we set the charge detection threshold at 3000  $e^-$  for any energy deposition within 5 mm. The corresponding energy threshold is particle dependent, but it is approximately equaling to  $E_{\text{dep}} = 100$  keV for a MIP particle with  $R_c = 0.7$ . This charge threshold setting is inspired by the low energy studies in recent LArTPC experiments [37]. For light calorimetry, we assume each photon detector's detection threshold is much below one photoelectron, so there is no loss of light signal below the

threshold for GeV events.

*c. Nuclear breakup* Since argon has a composite nucleus, particles could inelastically scatter on Ar and break up the nucleus to produce protons, neutrons, pions, and so on. These secondary hadrons tend to interact with Ar and produce more hadrons, which result in a hadronic shower. While doing so, some energy of the particles is spent to overcome the nuclear binding energy and becomes part of the missing energy. Particularly, the fraction of energy spent on the invisible nuclear breakup could be 30%–50% for neutrons [38], since they are neutral particles and don't deposit energy directly. Moreover, the event-by-event fluctuation for nuclear breakup is large and often becomes the dominant factor in the resolution of energy reconstruction.

*d. Particle decay and others* There are several other mechanisms to generate missing energy. The most common one is the charged pion and muon decays where some energy is carried away by neutrinos that escape the detector. Negatively charged pions and muons can also be captured by the Ar nuclei, resulting in some missing energy when the nuclei de-excite [39]. Neutrons will capture on Ar after thermalization and release several  $\gamma$ -rays that add up to about 6 MeV, which become the “negative” missing energy, i.e. extra energy if the capture  $\gamma$ -rays are included in the calorimetry.

In the following, we use GeV electron neutrinos as a case study to estimate missing energy contribution and energy responses in LArTPC. Muon neutrinos are also studied with similar conclusions and not reported here. Energetic neutrinos from 0.5–5 GeV are sent into a LArTPC detector. This energy range is consistent with the wide-band neutrino beam planned with the DUNE experiment [22] and  $\nu_e$  is the main appearance signal in DUNE. The LAr volume is large enough so that all particle activities are contained. The  $\nu$ -Ar interaction is modeled by the GENIE neutrino event generator [40] version 2.12.10. Only the charged current (CC) interaction is simulated since this is the main detection channel in neutrino oscillation studies for flavor tagging. The propagation of the primary particles in LAr after the  $\nu_e$ -Ar CC interaction is performed through the *edep-sim* software package [41], which provides a convenient interface to Geant4. Geant4 version 4.10.3.p01b is used in this study. The energy depositions per 5 mm step (or less if the final step is shorter than 5 mm) along the particle trajectories are stored. The  $E_{\text{dep}}$  in each step is then converted to the charge and light signals in terms of the number of ionization electrons and scintillation photons, taking into account the recombination effect, based on the procedures described in Sec. II. The drift electric field is set to be 0.5 kV/cm to calculate the charge recombination factor  $R_c$ .

The number of scintillation photons after recombination ( $N_\gamma^r$ ) is further converted to the total number of detected photoelectrons ( $N_{pe}$ ) assuming an average absolute PCE of 0.8%. This PCE is based on a standalone Geant4 simulation study of the APEX design for DUNE

Phase-II far detectors [24], where the surface optical coverage is about 60% and the photon detector (X-Arapuca) efficiency is 2%. In the current APEX design, the PCE is non-uniform across the detector volume because of the specific placements of the photon detectors. However, in this study, we assume a uniform PCE as an ideal case. Under this PCE, the light yield is about 180 photoelectrons per MeV of deposited energy for a MIP. Event-by-event fluctuation is applied to  $N_{pe}$  assuming a Poisson distribution, although it does not contribute significantly to the energy resolution for GeV neutrino events at this light yield. Finally, the simulated  $N_e^r$  and  $N_{pe}$  are converted to the visible energy in charge ( $Q$ ) and light ( $L$ ) following Eq. 8.

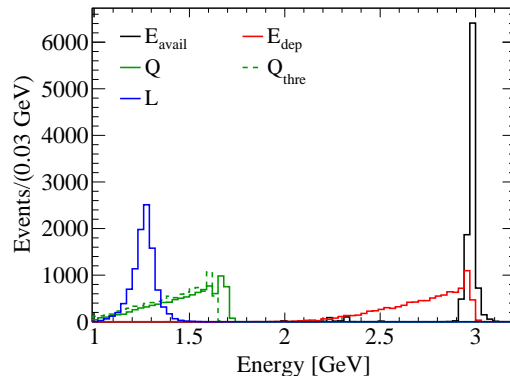


FIG. 3. Simulated distribution of energy dissipation from  $10^4$  3 GeV  $\nu_e$ -Ar CC interactions. Black histogram shows the distribution of the total available energy ( $E_{\text{avail}}$ ) of final state particles from the GENIE event generator. Red histogram shows the distribution of the deposited energy ( $E_{\text{dep}}$ ) in LAr. The green and blue histograms show the distributions of visible energy in charge ( $Q$ ) and light ( $L$ ), respectively, after the charge recombination. The dotted green histogram shows the distribution of  $Q$  after applying the charge detection threshold of 3000 ionization electrons.

Figure. 3 shows the simulated results for a 3 GeV electron neutrino, which is close to the peak energy of the DUNE neutrino beam. The  $\nu_e$ -Ar CC interaction can be generally written as:

$$\nu_e + Ar \rightarrow e^- + \pi^0\text{s} + \text{hadrons} + X, \quad (11)$$

where hadrons could include protons, neutrons, charged pions, and so on, and  $X$  is the nucleus after the interaction. Zero or more  $\pi^0$ s can be produced in the interaction and together with the electron from the  $\nu_e$ CC interaction, they form the electromagnetic activities in the event. In the GeV neutrino energy range, the  $\nu_e$ -Ar interaction cross section consists of several components such as the quasi-elastic scattering (QES), the  $\Delta$  resonance scattering (RES), the deep inelastic scattering (DIS), and so on. These interactions are modeled by the GENIE event generator to produce the final state particles and their kinematic distributions. The black histogram in Fig. 3 shows

the distribution of the total available energy ( $E_{\text{avail}}$ ) of the final state particles after the  $\nu_e$ -Ar interaction.  $E_{\text{avail}}$  includes the kinematic energy of stable or long-lived particles such as the protons, neutrons, and electrons, and the total energy of short-lived particles including their masses such as pions and muons. Some energy is missing at the  $\nu_e$ -Ar interaction due to nuclear breakup, but the energy smearing is relatively small at the neutrino generator level.

The red histogram in Fig. 3 shows the distribution of the deposited energy ( $E_{\text{dep}}$ ) in LAr. The missing energy is obvious at this step and the event-by-event fluctuation is large. The distribution has a long tail extending to lower energy, which is mostly caused by nuclear breakup when the primary or secondary hadrons, especially neutrons, inelastically scatter with Ar. This long low-energy tail creates an undesired feed-down effect in physics analysis since a high-energy neutrino event could appear at a much lower deposited energy.

The green and blue histograms in Fig. 3 show the visible energy measured in  $Q$  and  $L$ , respectively, with the simulation steps described earlier that include the recombination effect. The  $Q$  distribution (green) is relatively broader than the  $E_{\text{dep}}$  distribution (red), which is caused by the additional smearing from the  $dE/dx$  dependent charge recombination. The  $Q$  distribution after applying the charge detection threshold ( $3000 e^-$ ) is shown as the dotted green histogram, and the missing energy at this detection threshold is about 3%. Interestingly, the  $L$  distribution (blue) does not have the low-energy tail, is more symmetric, and has a much smaller event-by-event fluctuation than  $Q$ . The origin of this desired feature in LArTPC light calorimetry will be explored in Sec. IV.

Using the simulation results such as shown in Fig. 3, we can correct for the missing energy bias by applying an additional factor to scale the mean of each distribution ( $Q$ ,  $L$ , or  $E_{\text{dep}}$ ) to the initial neutrino energy  $E_\nu$ . The event-by-event fluctuation, however, cannot be corrected for and it contributes to the overall resolution of the energy reconstruction. The energy resolution is better using light calorimetry ( $L$ ) than the simple charge calorimetry ( $Q$ ), which will be further elaborated in Sec. IV. It is worth pointing out that the  $Q + L$  method using Eq. 10, while removing the recombination effect and recovering the  $E_{\text{dep}}$  distribution, does not significantly improve upon the charge-only calorimetry  $Q$ , because the missing energy contribution dominates the energy resolution. There are, however, other methods to further improve energy resolution in charge calorimetry by taking advantage of the imaging capability of LArTPC, which is not the main topic of this article and is described in Appendix C.

#### IV. SELF-COMPENSATING LIGHT CALORIMETRY

The features of the LArTPC light calorimetry seen in Fig. 3 can be understood in analogous to the *compensating calorimeter* concept in HEP accelerator experiments, which is an important technique because of the fundamental problems of hadron calorimetry [1, 42]. The development of hadronic cascades results in both the electromagnetic (EM) component and the hadronic component. The EM component ( $e$ ) comes from the  $\pi^0$  and  $\eta$  particles generated in the hadronic interactions, which decay into  $\gamma$ -rays that develop into EM showers. The hadronic component ( $h$ ) consists of everything else such as protons, neutrons, and charged pions. The calorimeter response ( $R_{\text{cal}}$ ), defined as the ratio of the visible energy to the available energy, is very different between  $e$  and  $h$ . As described in Sec. III B, missing energy due to nuclear breakup can be up to 30%–50% for hadrons with large event-by-event fluctuation, while for EM particles the response is typically higher with smaller fluctuations. A calorimeter is characterized by the  $e/h$  ratio, defined as the ratio between  $R_{\text{cal}}^e$  and  $R_{\text{cal}}^h$ . Calorimeters with  $e/h = 1$  are called compensating calorimeters. For non-compensating calorimeters, the response to the total energy depends on the fraction of visible energy in the EM component ( $f_{em}$ ), which has a large event-by-event fluctuation and often dominates the calorimeter energy resolution.

Compensation between the  $e$  and  $h$  responses is typically realized in sampling calorimeters using a combination of three techniques. First, the  $e$  response can be reduced by using high- $Z$  absorber materials. Second, the neutron response, which is a significant component in  $h$ , can be boosted by using hydrogenous active materials. Finally, the sampling fraction can be tuned to match  $e$  and  $h$  responses so that  $e/h = 1$ . Examples of high-performance compensating calorimeters include the ZEUS calorimeter at HERA using uranium absorbers and plastic scintillators [43], and the Spaghetti Calorimeter (SPACAL) at CERN using lead absorbers and scintillation fibers [44].

In a LArTPC neutrino detector, the  $\nu_e$ CC interaction (Eq. 11) guarantees there are both EM (electrons and possibly  $\pi^0$ s) and hadronic components in the calorimeter. The fraction of EM component ( $f_{em}$ ) varies event-by-event and is energy-dependent, which is modeled by the neutrino event generator such as GENIE. Similar to the problems of hadron calorimeters mentioned previously, if the LArTPC's calorimeter response ( $R_{\text{cal}}$ ) between  $e$  and  $h$  is very different, the fluctuation of  $f_{em}$  will largely impact the calorimeter energy resolution and the shape of the energy response. The calorimeter responses in LArTPC are studied with the detector simulation described in Sec. III B. For each  $\nu_e$ CC event, the electron and  $\pi^0$ s, if any, are grouped into  $e$ , and the protons, neutrons, pions, and other final-state particles are grouped into  $h$ .  $R_{\text{cal}}$  in each component is calculated

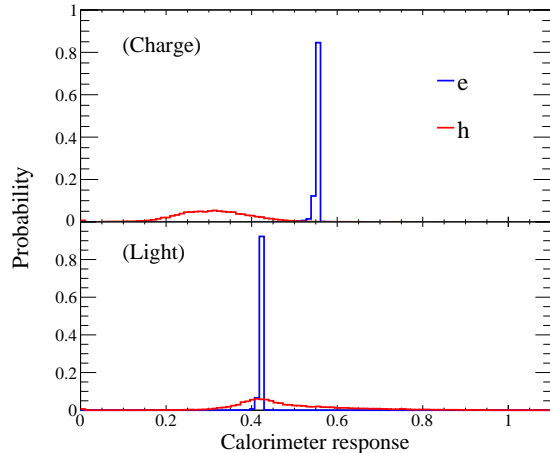


FIG. 4. The calorimeter responses ( $R_{\text{cal}}$ , the ratio of the visible energy to the available energy) in LArTPC for the EM component ( $e$ , blue) and the hadronic component ( $h$ , red). The top panel shows the charge calorimetry and the bottom panel shows the light calorimetry.  $10^5$   $\nu_e$  CC events are simulated with neutrino energy of 0.5–5 GeV. The area of each distribution is normalized to 1.

and plotted in Fig. 4. The top panel shows the  $e$  (blue) and  $h$  (red) responses in the charge calorimetry and the bottom panel shows the light calorimetry. The event-by-event fluctuation in the  $e$  responses is much smaller than the  $h$  responses because of the much smaller contribution of missing energy in  $e$ . The most interesting feature, however, is that the peak of  $e/h$  in the light calorimetry is close to 1, which makes LArTPC a *self-compensating* light calorimeter.

The self-compensation mechanism in the scintillation light can be understood by rewriting the calorimeter response in two terms:

$$R_{\text{cal}} = \frac{\sum E_{\text{vis}}}{\sum E_{\text{dep}}} \cdot \frac{\sum E_{\text{dep}}}{\sum E_{\text{avail}}} = \begin{cases} \overline{\beta R_c} \cdot \bar{R}_{\text{dep}}, & (\text{charge}) \\ \overline{R_L} \cdot \bar{R}_{\text{dep}}, & (\text{light}) \end{cases} \quad (12)$$

where the summation is over all particles in each component,  $e$  or  $h$ . The first term in Eq. 12 is the average charge or light recombination factor, and the second term is the average ratio of the deposited energy to the total available energy. The two terms are plotted in Fig. 5 for  $e$  (blue solid circles) and  $h$  (red crosses) separately from 1000 simulated 3 GeV  $\nu_e$ -Ar CC events, where the charge response is shown in the top panel and the light response is shown in bottom. The  $\bar{R}_{\text{dep}}$  is close to 1 for  $e$  and  $\sim 0.7$  for  $h$ , showing that the missing energy fraction is significant in  $h$ . On the other hand, the light recombination factor ( $R_L$ ), based on Eq. 7 and Fig. 2, is larger for  $h$  than  $e$  because of the higher  $dE/dx$  for heavily ionizing particles such as protons in  $h$ . The extra scintillation light from recombination compensates for the larger missing energy in  $h$ , resulting in both the  $e$  and  $h$  responses centralized around the  $R_{\text{cal}} = xy = 0.42$  curve in Fig. 5, making

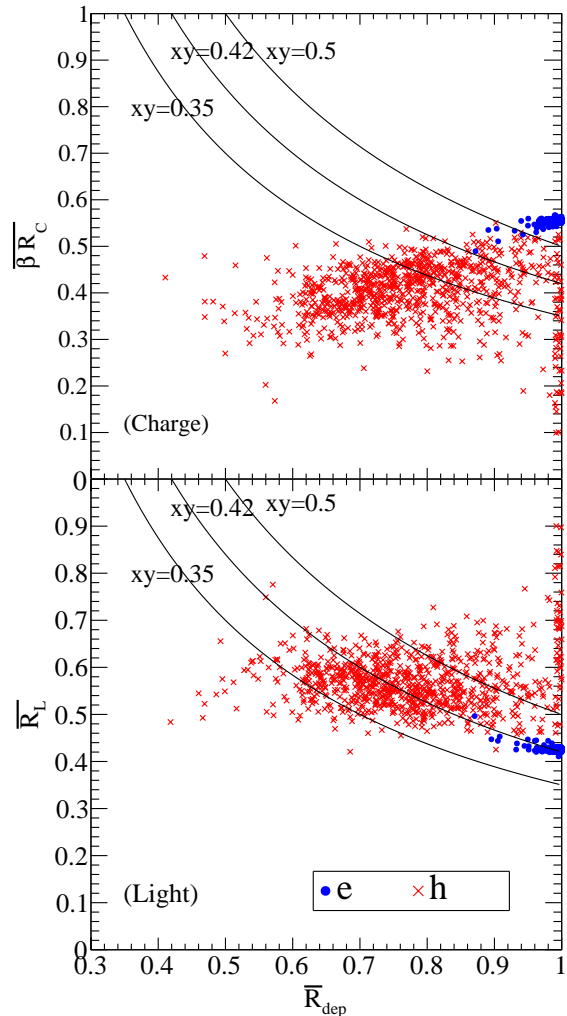


FIG. 5. A scatter plot of 1000 simulated 3 GeV  $\nu_e$ -Ar CC events in a LArTPC. Activities in each event are grouped into the EM ( $e$ , solid circles) and hadronic ( $h$ , crosses) components. The y-axis shows the average recombination factor for charge ( $\beta R_c$ , top) or light ( $R_L$ , bottom) in  $e$  (blue solid circles) or  $h$  (red crosses). The x-axis shows the average ratio of the deposited energy to the total available energy in  $e$  or  $h$ . The product of  $x$  and  $y$  is the calorimeter response shown in Fig. 4, where the  $xy = 0.42$  curve corresponds to the peak position of the  $e$  or  $h$  distribution in the light calorimeter response (bottom panel of Fig. 4).

$e/h$  close to 1 in the light calorimetry. This effect, however, is anti-compensating for ionization electrons since the charge recombination factor  $R_c$  is smaller for  $h$  than  $e$ , making  $e/h$  close to 1.8 in the charge calorimetry.

The compensation performance of the LArTPC light calorimetry is dependent on the size of the drift electric field. The top panel of Fig. 6 shows the light recombination factor ( $R_L$ ) as a function of the drift electric field derived from Eq. 6 and 7. The different colored curves show the  $R_L$  for particles with  $dE/dx$  equaling to 1, 2,

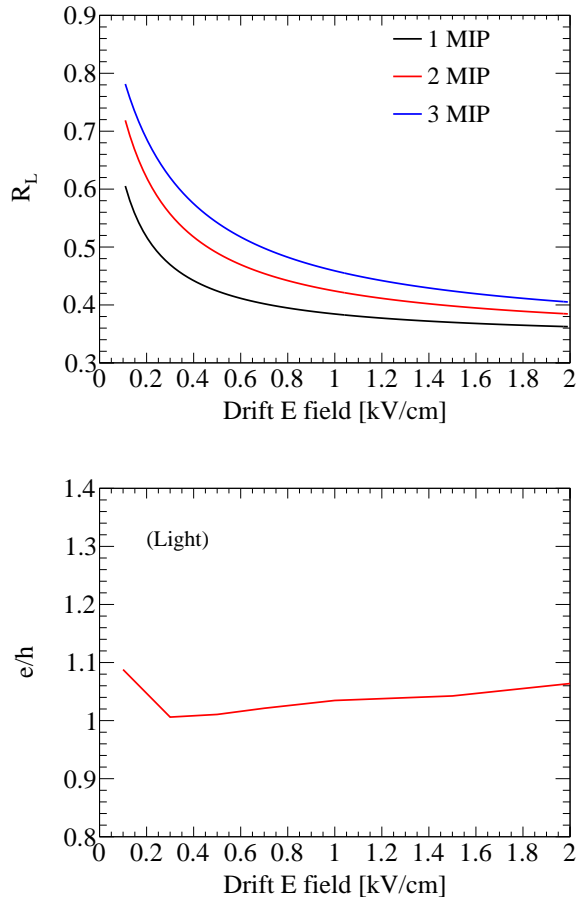


FIG. 6. (Top) The light recombination factor ( $R_L$ ) as a function of the drift electric field. The three curves correspond to particles with  $dE/dx$  equaling to 1, 2, and 3 times that of a minimum ionizing particle (2.1 MeV/cm), respectively. (Bottom) The calorimeter response ratio between  $e$  and  $h$  ( $e/h$ ) as a function of the drift electric field.

and 3 times that of a MIP ( $dE/dx = 2.1$  MeV/cm). At a fixed drift E-field, the more separated are  $R_{LS}$ , the more compensation there is between the  $e$  and  $h$  responses. The  $e/h$  is calculated at each E-field, and the optimal compensation of  $e/h$  close to 1 can be achieved between 0.3–0.5 kV/cm. The compensation is slightly worse at lower and higher E-fields, but  $e/h$  between 1–1.05 can still be achieved across a broad range of E-fields between 0.2–1.8 kV/cm.

The compensation performance in the light calorimetry is also energy-dependent. To study the energy dependence, the events in Fig. 4 are divided into different incident neutrino energy bins, and the calorimeter response of the hadronic component ( $R_{\text{cal}}^h$ ) in the light calorimetry is plotted in Fig. 7. For neutrino energies greater than 2 GeV, the  $R_{\text{cal}}^h$  distributions are similar, with smaller fluctuations for higher energy neutrinos. The  $R_{\text{cal}}^h$  distribution, however, is much wider for the 1 GeV or lower-energy incident neutrinos, which leads to

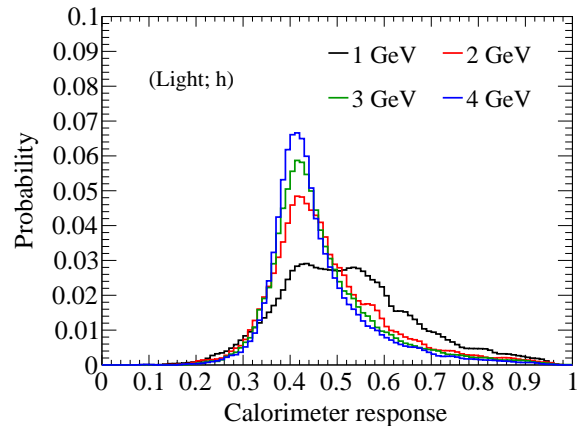


FIG. 7. The calorimeter response of the hadronic component  $h$  in the light calorimetry at different incident neutrino energies.

a worse reconstructed energy resolution for lower-energy neutrinos (cf. Fig. 9) using light calorimetry.

This energy dependence is further studied in Fig. 8 by separately plotting the  $R_{\text{cal}}$  for protons, neutrons, and charged pions in the light calorimetry. The top panel shows a scatter plot of the available energy of each particle (i.e. the kinetic energy of protons and neutrons, and the total energy of the charged pions) versus its  $R_{\text{cal}}$ . The bottom panel shows the projected distribution of  $R_{\text{cal}}$  for different particles for all energies. We can observe that at low energy below  $\sim 1$  GeV, the behavior is quite different between  $p$ ,  $n$ , and  $\pi^\pm$ . This is because a large contribution of  $R_{\text{cal}}$  comes from the primary particle itself before it possibly starts a hadronic shower. Proton has a higher  $R_{\text{cal}}$  because it starts as a charged particle without missing energy, and receives extra recombination light. Neutron has a lower  $R_{\text{cal}}$  because it has a high missing energy from the beginning. Charge pion has a similar  $dE/dx$  as a MIP particle before it starts the hadronic shower, so its  $R_{\text{cal}}$  is similar to electrons, with additional missing energy from particle decays. Therefore, the total  $R_{\text{cal}}$  of the hadronic component becomes dependent on the distribution of final state particles, leading to a wider distribution for lower energy neutrinos as seen in Fig. 7. However, at higher energy above  $\sim 2$  GeV, the  $p$ ,  $n$ , and  $\pi^\pm$  behave very similarly because they all start hadronic cascades and the  $R_{\text{cal}}$  is dominated by the secondary shower particles, which are similar for different primary particles. Thus, the compensation performance is better for higher-energy neutrinos and less sensitive to the modeling of final-state particles after neutrino interactions.



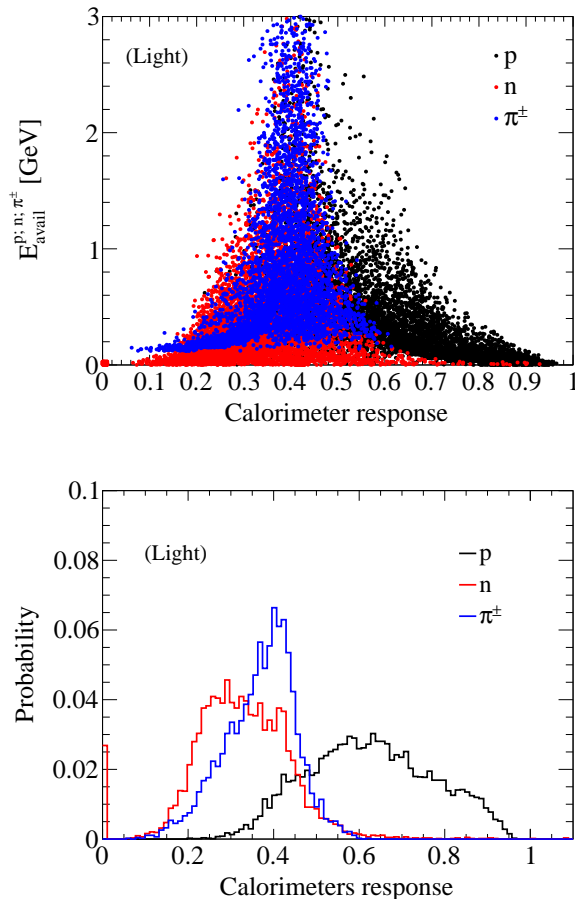


FIG. 8. The calorimeter response ( $R_{\text{cal}}$ ) for protons, neutrons, and charged pions in the light calorimetry. The top panel shows a scatter plot of the available energy of each particle versus its  $R_{\text{cal}}$ . The bottom panel shows the projected distribution of  $R_{\text{cal}}$  of different particles for all energies.

## V. ENERGY RESOLUTION COMPARISON

Based on the discussions in Sec. IV and Appendix C, in this section, we describe four energy reconstruction methods in LArTPC, one for light calorimetry and three for charge calorimetry, and compare their performance. The light calorimetry utilizes the self-compensating calorimeter concept first described in this paper. The charge calorimetry methods are similar in concept to previous works from LArTPC experiments and are included here for comparison.

1. *L1*: Simple light calorimetry by summing up  $L$  from all particle activities and scaling to the incident neutrino energy:

$$E_{\text{rec}}^{L1} = \frac{L}{0.42}. \quad (13)$$

2. *Q1*: Simple charge calorimetry by summing up  $Q$

from all particle activities and scaling to the incident neutrino energy:

$$E_{\text{rec}}^{Q1} = \frac{Q}{0.48}. \quad (14)$$

3. *Q2*: Assuming  $e$  and  $h$  charge activities can be grouped using pattern recognition algorithms on the 3D image (cf. Appendix C), scaling the  $Q$  from  $e$  and  $h$  separately before summing up to the incident neutrino energy:

$$E_{\text{rec}}^{Q2} = \frac{Q_e}{0.55} + \frac{Q_h}{0.31}. \quad (15)$$

4. *Q3*: On top of *Q2*, assuming tracks longer than 2 cm can be reconstructed and the  $dE/dx$  along the tracks can be measured, the  $E_{\text{dep}}$  of the tracks can then be faithfully reconstructed by correcting for the charge recombination factors along the tracks. For the rest of the dot-like activities, scale the  $Q$  from  $e$  and  $h$  separately similar to *Q2*:

$$E_{\text{rec}}^{Q3} = E_{\text{dep}}^{\text{tracks}} + \frac{Q_e^{\text{dots}}}{0.47} + \frac{Q_h^{\text{dots}}}{0.20}. \quad (16)$$

The scaling factors used in each reconstruction come from the detector simulation described in Sec. III B, which account for both the recombination effect and the missing energy contributions.

We also studied two additional reconstruction methods but they are not reported in detail here. The first method is the  $Q+L$  calorimetry based on Eq. 8. While it removes the recombination effect and recovers  $E_{\text{dep}}$ , it does not account for the missing energy contribution, therefore, its performance is only slightly better than *Q1* but worse than *Q2* and *L1*. The second method assumes activities from individual particles can be grouped and their energies can be reconstructed separately. This is mostly useful for muons and charged pions since their missing energies from decays or captures can be corrected event-by-event, using methods such as a range-based energy reconstruction. The missing energy fluctuation from nuclear breakup still remains, e.g. from neutrons, making its performance only slightly better than *Q3*.

The top panel of Fig. 9 shows the distribution of the reconstructed neutrino energy from  $10^4$  simulated 3 GeV  $\nu_e$ -Ar CC interactions using the *Q1*–*3* and *L1* reconstruction methods. *Q1* (black) has a long tail extending to low energies, which comes from the missing energy contribution and the different calorimeter response between  $e$  and  $h$ . *L1* (red) removes the low-energy tail through the self-compensation mechanism, resulting in a more symmetric shape and much better resolution. *Q2* (green) has a similar performance as *L1*, sharper near the peak but with a longer tail in the high energy. *Q3* (blue) has the best overall performance. Both *Q2* and *Q3* utilize LArTPC's charge imaging capability to separate  $e$  and  $h$  activities to improve the reconstructed energy resolution.

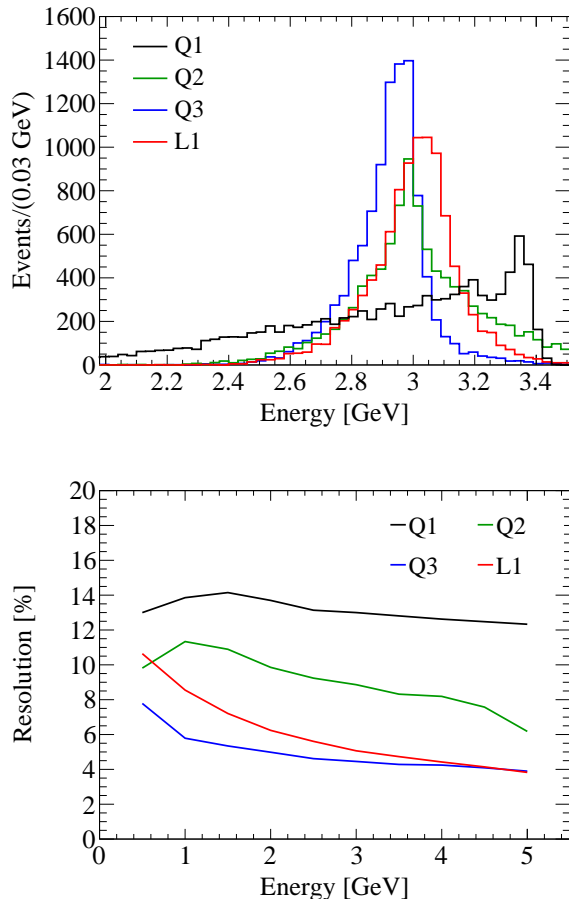


FIG. 9. (top) The distribution of the reconstructed neutrino energy from  $10^4$  simulated 1 GeV  $\nu_e$ -Ar CC interaction events. The four colored histograms correspond to the four reconstruction methods Q1–3 and L1, respectively. (bottom) The relative energy resolution,  $\sigma/\bar{E}$ , as a function of the incident neutrino energy for the four reconstruction methods Q1–3 and L1.

The bottom panel of Fig. 9 shows the relative energy resolution,  $\sigma/\bar{E}$ , as a function of the incident neutrino energy. For each fixed neutrino energy, the  $\sigma$  is calculated from the root mean square (RMS) of the distribution from each reconstruction method, and the mean energy of the distribution is used as  $\bar{E}$ . The RMS is larger than the width of the peak for a tailed distribution such as Q1 and Q2. This plot shows that Q3 achieves the best energy resolution at  $\sim 6\%$  at 1 GeV and Q1 has the worst resolution of  $\sim 14\%$  at 1 GeV. The L1 method has an 8.4% resolution at 1 GeV. The Q2 method performs similarly to L1, although the longer tail at high energy makes its RMS worse than L1. In practice, the 2D energy response matrices of reconstructed neutrino energy vs. true neutrino energy, also called the detector smearing matrices, are used in physics analysis, and they are shown in Fig. 11 in Appendix D. The energy resolution and response matrices from this study can be readily compared with other

literature or experimental works [22, 38, 45–47], and can be used in the phenomenology studies such as those in Ref. [45, 48]. One should keep in mind the experimental conditions assumed in different studies.

It’s worth noting that although Q3 has the best overall performance, the light calorimetry L1 is a much simpler reconstruction method without needing complex pattern recognition algorithms to separate  $e$  versus  $h$ , or track-like versus dot-like activities. For higher energy neutrinos above 3 GeV, the performance between L1 and the much more sophisticated Q3 methods nearly equals owing to the self-compensation mechanism in the light calorimetry. Therefore, the light calorimetry in LArTPC provides an independent and comparable energy estimation, complementing the well-established charge calorimetry. The synergy between the light and charge calorimetry offers a novel approach to evaluating and mitigating the systematic uncertainties in energy measurements with LArTPCs.

## VI. DISCUSSIONS AND OUTLOOK

In this work, we reviewed LArTPC’s capability as a dual calorimeter to estimate the energy of incident particles using the ionization charge and the scintillation light. Because of the charge recombination and the light generation mechanisms involved in the energy dissipation in LAr, the light calorimetry in LArTPC is inherently self-compensating. Good compensation of  $e/h$  close to 1 can be achieved in a wide range of drift E-field from 0.2–1.8 kV/cm. Using the GeV neutrinos as a case study, we demonstrate that light calorimetry can achieve a comparable energy resolution as the more sophisticated charge imaging calorimetry, which requires pattern recognition algorithms to separate particle activities.

We made a few simplifications in this study. The LArTPC is assumed to be infinitely large so that all particle activities (except neutrinos) are contained. For finite-sized detectors, the missing energy from partially contained particles should be studied. The LArTPC is assumed to be fully active, which is not the case for detectors with multiple drift volumes. The active volume for charge and light calorimetry is assumed to be the same, but scintillation light can also be generated in LAr outside of the TPC active volume. The light yield is assumed to be uniform across the entire detector, which in practice is difficult to achieve because of the constraints of photon detector placement and achievable surface coverage. The scintillation light is assumed to be fully collected regardless of its time distribution, but the late light component could play an important role in the photon signal reconstruction and affect the calorimeter response [49]. Other contributions to energy resolution such as electronic noise, constant backgrounds, and channel-to-channel variations, are also ignored in this work. While the event-by-event fluctuation in the missing energy is often the dominating factor in the energy

resolution, these other contributors could still play a large role if the detector design is not optimized for energy resolution. Therefore, the results from this work can be viewed as an optimal case for the performance of dual calorimetry in LArTPC. Dedicated simulation and analysis studies are necessary to understand all contributions to energy resolution for specific detector designs.

The results from this work can have many applications:

1. As a theoretical framework to properly implement scintillation light simulation in LArTPC experiments. While comprehensive models, such as NEST [50], to simulate the scintillation yield of noble liquids are popular in dark matter experiments, the light simulation in most of the current LArTPC neutrino experiments is less sophisticated without considering recombination luminescence. This work demonstrates why a proper light simulation is important in LArTPC light calorimetry and outlines the detailed implementation procedures.
2. As a motivation and guidance to perform light calorimetry in LArTPC experiments for GeV neutrino physics. In most of the current LArTPC neutrino experiments, scintillation light is only used to provide the  $t_0$  and trigger information. Light calorimetry to improve MeV neutrino physics has been suggested [22], but the motivation to conduct high-energy light calorimetry is lacking. This work demonstrates that in a LArTPC experiment with a capable light detection system, light calorimetry can provide an independent energy measurement with a comparable performance to the more sophisticated charge imaging calorimetry for GeV neutrinos. This will benefit numerous physics programs, such as long-baseline neutrino oscillations, atmospheric neutrinos, tau neutrino physics, and many others.
3. As a new approach to evaluating and mitigating the systematic uncertainties in energy measurements with LArTPCs. The systematic uncertainty associated with neutrino energy reconstruction is one of the largest uncertainties affecting the measurements of neutrino oscillation parameters and  $\nu$ -Ar cross sections. Two main contributors to the uncertainty in neutrino energy reconstruction are 1) mistakes in the pattern recognition algorithms when analyzing the charge-based images, and 2) dependence on the final state particle distribution provided by  $\nu$ -Ar interaction event generator models. The simplistic nature of the light calorimetry and the less dependence on the final state distribution (cf. Sec. IV) provides a novel way to tackle this problem.
4. As a foundational model to be tested. The self-compensation mechanism described in this work can be readily tested in the current and future LArTPC experiments with capable light detection systems, such as ICARUS [19], SBND [20], the DUNE LAr near detector modules [23], and the DUNE far detector pro-

totypes [21, 24]. Care should be taken to calibrate the photon detector response and correct for effects such as the light collection non-uniformity, time integration dependence, and the selection of events.

5. As a design direction to improve light detection capability in future LArTPC experiments. Optimized photon detector designs, such as the APEX detector concept, are being carried out in the DUNE Phase-II program [24] for the next far detectors to improve their light detection capability such as optical coverage, photon collection efficiency, uniformity of the light response, position resolution, among others. While the original purpose for such an upgrade was to improve DUNE's lower energy physics program such as nucleon decay, supernova neutrino detection, and solar neutrinos, the results from this work provide another strong motivation and reference on how to optimize the photon detector system design to further enhance DUNE's capability in long-baseline neutrino oscillation and other high-energy physics programs.
6. As a starting point for works beyond neutrino physics. While this work focuses on the energy reconstruction of few-GeV neutrinos, it can be extended to the calorimetry of higher energy particles since the principles presented are general. The self-compensation mechanism in the LArTPC light calorimetry provides a new way to build compensating calorimeters without reducing the performance of EM responses. Coupled with the sampling calorimeter technology to contain the particle activities in a small LArTPC, scintillation light calorimetry could be considered on its own or in complementary to the well-established ionization charge calorimetry as the next-generation calorimeter for high energy collider experiments. Dedicated simulation studies are necessary to optimize its design to reach the best achievable energy resolution.

While LArTPC has been traditionally considered only as a charge-based calorimeter for GeV neutrino physics, we hope this work has proven its tremendous potential as a scintillation light calorimeter and serves as a stepping stone for future applications of light calorimetry with LArTPCs.

## ACKNOWLEDGMENTS

We thank Xin Qian and Milind Diwan for providing valuable discussions on this research. This work is supported by the US Department of Energy (DOE) Office of Science, Office of High Energy Physics under Contract No. DE-SC0012704, DE-SC0009854, BNL LDRD 23-058, and 2024 SBU-BNL Seed Grant Program.

## Appendix A: List of symbols

Table I lists the symbols used in this article, including their values, definitions, and descriptions.

Symbol	Value	Description
$E_{\text{avail}}$		total available energy
$E_{\text{dep}}$		deposited energy in LAr
$N_e$	(4)	number of ionization electrons
$N_\gamma$	(4)	number of scintillation photons
$N_e + N_\gamma$		total number of quanta
$\alpha$	0.21	$N_\gamma/N_e$
$\beta$	0.83	$1/(1 + \alpha)$
$W_{\text{ph}}$	19.5 eV	energy to create one quantum
$W_{\text{ion}}$	23.6 eV	$W_{\text{ph}}/\beta$
$R_c$	(6)	charge recombination factor
$R_L$	(7)	light recombination factor
$N_e^r$		$N_e R_c$
$N_\gamma^r$		$(N_e + N_\gamma) R_L$
$E_{\text{vis}}$		visible energy
$Q$	(8)	visible energy in charge
$L$	(8)	visible energy in light
$R_{\text{cal}}$	$E_{\text{vis}}/E_{\text{avail}}$	calorimeter response
$e$		EM component
$h$		hadronic component
$e/h$		$R_{\text{cal}}^e/R_{\text{cal}}^h$
$E_{\text{rec}}$		reconstructed energy

TABLE I. List of symbols used in this article.

## Appendix B: Quanta reducing processes

There are three main processes that could reduce the total number of quanta ( $N_e + N_\gamma$ ) in a LArTPC. However, all of them can be neglected in the scope of this work:

*a. Escaping electrons* At zero electric field, the photon yield was observed to be only about 40000 photons per MeV, i.e.  $\sim 78\%$  of the ideal photon yield [26, 51]. This effect was attributed to the “escaping electrons” — some electrons are thermalized outside of the ion-influence radius and can live for a long time ( $>$  milliseconds) without recombination, thus escaping the light collection time window. This effect diminishes once a drift electric field is applied, where the escaping electrons are collected as charge signals.

*b. Scintillation quenching* It was observed that for  $\alpha$  particles, Au ions, and fission fragments at high LET, the total quanta ( $N_e + N_\gamma$ ) collected is only about 20–70% of the ideal yield. This was explained by the biexcitonic quenching model [52], where two  $\text{Ar}^*$  atoms can combine and de-excite non-radiatively, i.e. dissipate their energy through heat. The biexcitonic quenching factor not only depends on LET, but also on the track microscopic structure such as the radial distribution of the energy deposition. While this is an important systematic effect for nuclear recoil in low energy dark matter experiments, the biexcitonic quenching was calculated to be

negligible for relativistic particles and for few-MeV protons [52]. Therefore, we have neglected the scintillation quenching in our studies focusing on the calorimetry of GeV particles (and their secondaries). A second type of scintillation quenching happens when there exists parts-per-million level nitrogen contamination in LAr. In this case, the  $\text{Ar}_2^*$  excimer states could de-excite by collision with  $\text{N}_2$  molecules [53], thus reducing the scintillation light yield. We assume the nitrogen impurity can be well controlled and do not consider this type of scintillation quenching in this work.

*c. Electron attachment* Ionization electrons could attach to electronegative impurities in LAr and form negative ions during their passage to the anodes. Since the drift velocity of ions is about five orders of magnitude lower than that of electrons, these ions escape the charge collection and the original signal is attenuated as a function of drift distance. Common electronegative impurities in LAr are the oxygen and water molecules. The electron attachment rates for different impurities are summarized in Ref. [54]. For large LArTPCs, purification of LAr to remove  $\text{O}_2$  and  $\text{H}_2\text{O}$  is essential to allow a long drift distance of a few meters without significant signal attenuation. Parts-per-trillion level impurity and electron lifetime of more than 3 ms have been successfully demonstrated in recent experiments such as MicroBooNE [18] and ProtoDUNE-SP [21], so in this work we assume the electron attenuation from attachment to impurities is negligible.

## Appendix C: Charge imaging calorimetry

In Sec. IV, we explain that in calorimeters where the  $e$  and  $h$  responses are very different, the event-by-event fluctuation in  $f_{em}$  could largely impact the resolution of the reconstructed energy. Compensating calorimeters, such as the LArTPC light calorimetry described therein, mitigate this issue by making  $e/h$  close to 1. An alternative approach is to measure the  $e$  and  $h$  components separately, and apply the calorimeter response corrections accordingly:

$$E_{\text{rec}} = \frac{E_{\text{vis}}^e}{R_{\text{cal}}^e} + \frac{E_{\text{vis}}^h}{R_{\text{cal}}^h}, \quad (\text{C1})$$

where  $E_{\text{rec}}$  is the reconstructed energy of the incident particles. In the past HEP accelerator experiments, one way to achieve this is using dual-readout calorimeters that measure both the scintillation and the Cerenkov light [55, 56]. Since most of the deposited energy in a hadronic shower is by non-relativistic particles such as low-energy protons, the Cerenkov calorimeter is less responsive to  $h$ . Therefore, by measuring both the scintillation and the Cerenkov light, the  $f_{em}$  can be deduced event-by-event, and the  $e$  and  $h$ 's calorimeter responses can be applied separately.

In a LArTPC, the  $e$  and  $h$  activities in ionization electrons can be naturally separated utilizing LArTPC's su-

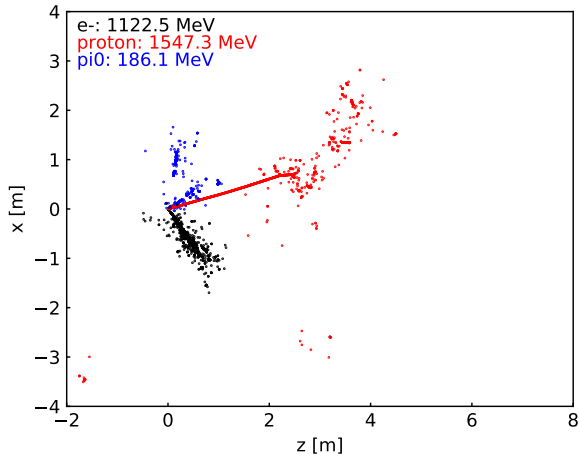


FIG. 10. An example 2D event display of a simulated 3 GeV  $\nu_e$  CC interaction in LArTPC. Different colors represent the activities from different primary particles generated by the neutrino interaction.

perb 3D imaging capability with mm-scale position resolution. Figure 10 shows an example 2D event display of a simulated  $\nu_e$ -Ar CC interaction in LArTPC. Colors represent activities from different primary particles generated by the neutrino interaction. In this example, an electron, a  $\pi^0$ , and a proton are generated after the interaction, and the particles further develop into EM and hadronic showers in the detector. With dedicated LArTPC pattern recognition algorithms such as WireCell [57], Pandora [58], Deep Learning [59], among others, the  $e$  (e.g. the electron activities in black and the  $\pi^0$  activities in blue) and  $h$  (e.g. the proton activities in red) components can be grouped separately, and Eq. C1 can be used to reconstruct the neutrino energy. This method, also called the *charge imaging calorimetry*, is adopted by most of the current LArTPC experiments for energy reconstruction, which can achieve better performance than the simple charge calorimetry by adding up all charges.

The charge imaging calorimetry can be further improved by correcting for the  $dE/dx$  dependent recombination factor  $R_c$  event-by-event, where the fluctuation, in particular in  $h$ , could be large, as illustrated in Fig. 5. The  $dE/dx$  can be calculated by reconstructing all track-

like objects and measuring the  $dE$  for each segment of  $dx$  along the reconstructed trajectories. Then, the deposited energy for track-like objects can be faithfully reconstructed using Eq. 9. However, if the track is too short, it becomes a dot-like object and the  $dE/dx$  cannot be well measured since the  $dx$  is difficult to reconstruct. Short tracks are commonly seen in the EM and hadronic showers that create many low-energy particles. The capability to reconstruct short tracks depends on the position resolution of the LArTPC, which typically has a pitch size of 3–5 mm and a track of a few centimeters can be well reconstructed. The separation of track-like and dot-like objects has been achieved by dedicated pattern recognition algorithms, in particular with the recent advancement in deep learning neural networks [60, 61]

#### Appendix D: Detector smearing matrix

Figure 11 shows the detector smearing matrices of reconstructed neutrino energy vs. true neutrino energy for  $\nu_e$ s. The four subplots are for the four reconstruction methods Q1–3 and L1, respectively. The smearing matrices for  $\bar{\nu}_e$ s are similar and not shown here.

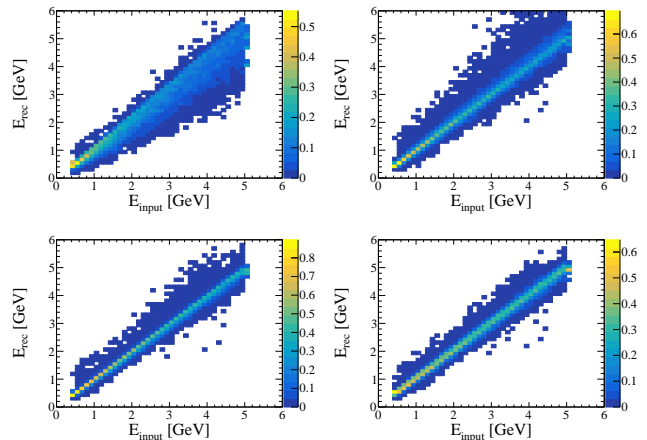


FIG. 11. The detector smearing matrices of reconstructed neutrino energy vs. true neutrino energy for electron neutrinos. The four subplots are for the four reconstruction methods Q1 (top left), Q2 (top right), Q3 (bottom left), and L1 (bottom right), respectively.

[1] C. W. Fabjan and F. Gianotti, Calorimetry for particle physics, *Rev. Mod. Phys.* **75**, 1243 (2003).  
 [2] W. Willis and V. Radeka, Liquid Argon Ionization Chambers as Total Absorption Detectors, *Nucl. Instrum. Meth.* **120**, 221 (1974).  
 [3] W. M. Bonivento and F. Terranova, The science and technology of liquid argon detectors, (2024), arXiv:2405.01153 [physics.ins-det].

[4] L. Apanasevich *et al.* (E706), Calibration and performance of the E706 lead and liquid argon electromagnetic calorimeter, *Nucl. Instrum. Meth. A* **417**, 50 (1998).  
 [5] D. Axen *et al.*, The Lead liquid argon sampling calorimeter of the SLD detector, *Nucl. Instrum. Meth. A* **328**, 472 (1993).  
 [6] S. Abachi *et al.* (D0), Beam tests of the D0 uranium liquid argon end calorimeters, *Nucl. Instrum. Meth. A*

- 324**, 53 (1993).
- [7] B. Andrieu *et al.* (H1 Calorimeter Group), The H1 liquid argon calorimeter system, Nucl. Instrum. Meth. A **336**, 460 (1993).
- [8] ATLAS liquid argon calorimeter: Technical design report, (1996).
- [9] R. Ajaj *et al.* (DEAP), Search for dark matter with a 231-day exposure of liquid argon using DEAP-3600 at SNOLAB, Phys. Rev. D **100**, 022004 (2019), arXiv:1902.04048 [astro-ph.CO].
- [10] R. Acciarri *et al.*, The WArP experiment, J. Phys. Conf. Ser. **203**, 012006 (2010).
- [11] P. Agnes *et al.* (DarkSide), First Results from the DarkSide-50 Dark Matter Experiment at Laboratori Nazionali del Gran Sasso, Phys. Lett. B **743**, 456 (2015), arXiv:1410.0653 [astro-ph.CO].
- [12] C. E. Aalseth *et al.* (DarkSide-20k), DarkSide-20k: A 20 tonne two-phase LAr TPC for direct dark matter detection at LNGS, Eur. Phys. J. Plus **133**, 131 (2018), arXiv:1707.08145 [physics.ins-det].
- [13] V. Fanti *et al.* (NA48), The Beam and detector for the NA48 neutral kaon CP violations experiment at CERN, Nucl. Instrum. Meth. A **574**, 433 (2007).
- [14] A. M. Baldini *et al.* (MEG), Search for the lepton flavour violating decay  $\mu^+ \rightarrow e^+\gamma$  with the full dataset of the MEG experiment, Eur. Phys. J. C **76**, 434 (2016), arXiv:1605.05081 [hep-ex].
- [15] C. Rubbia, The Liquid Argon Time Projection Chamber: A New Concept for Neutrino Detectors, CERN-EP-INT-77-08, CERN-EP-77-08 (1977).
- [16] H. Chen, P. Condon, B. Barish, and F. Sciulli, A Neutrino detector sensitive to rare processes. I. A Study of neutrino electron reactions, FERMILAB-PROPOSAL-0496 (1976).
- [17] S. Amerio *et al.* (ICARUS), Design, construction and tests of the ICARUS T600 detector, Nucl. Instrum. Meth. A **527**, 329 (2004).
- [18] R. Acciarri *et al.* (MicroBooNE), Design and Construction of the MicroBooNE Detector, JINST **12** (02), P02017, arXiv:1612.05824 [physics.ins-det].
- [19] L. Bagby *et al.* (ICARUS-T600), Overhaul and Installation of the ICARUS-T600 Liquid Argon TPC Electronics for the FNAL Short Baseline Neutrino Program, JINST **16** (01), P01037, arXiv:2010.02042 [physics.ins-det].
- [20] R. Acciarri *et al.* (SBND), Construction of precision wire readout planes for the Short-Baseline Near Detector (SBND), JINST **15** (06), P06033, arXiv:2002.08424 [physics.ins-det].
- [21] A. A. Abud *et al.* (DUNE), Design, construction and operation of the ProtoDUNE-SP Liquid Argon TPC, JINST **17** (01), P01005, arXiv:2108.01902 [physics.ins-det].
- [22] B. Abi *et al.* (DUNE), Deep Underground Neutrino Experiment (DUNE), Far Detector Technical Design Report, Volume II: DUNE Physics, (2020), arXiv:2002.03005 [hep-ex].
- [23] A. Abed Abud *et al.* (DUNE), Performance of a modular ton-scale pixel-readout liquid argon time projection chamber, (2024), arXiv:2403.03212 [physics.ins-det].
- [24] A. Abed Abud *et al.* (DUNE), DUNE Phase II: Scientific Opportunities, Detector Concepts, Technological Solutions, (2024), arXiv:2408.12725 [physics.ins-det].
- [25] T. Doke, Fundamental Properties of Liquid Argon, Krypton and Xenon as Radiation Detector Media, Portugal. Phys. **12**, 9 (1981).
- [26] T. Doke, K. Masuda, and E. Shibamura, Estimation of absolute photon yields in liquid argon and xenon for relativistic (1 MeV) electrons, Nucl. Instrum. Meth. A **291**, 617 (1990).
- [27] E. Segreto, Properties of Liquid Argon Scintillation Light Emission, Phys. Rev. D **103**, 043001 (2021), arXiv:2012.06527 [physics.ins-det].
- [28] T. Takahashi, M. Miyajima, S. Konno, T. Hamada, S. Kubota, H. Shibamura, and T. Doke, The w-value of liquid argon, Physics Letters A **44**, 123 (1973).
- [29] T. Doke, A. Hitachi, J. Kikuchi, K. Masuda, H. Okada, and E. Shibamura, Absolute Scintillation Yields in Liquid Argon and Xenon for Various Particles, Jap. J. Appl. Phys. **41**, 1538 (2002).
- [30] S. Kubota, A. Nakamoto, T. Takahashi, T. Hamada, E. Shibamura, M. Miyajima, K. Masuda, and T. Doke, Recombination luminescence in liquid argon and in liquid xenon, Phys. Rev. B **17**, 2762 (1978).
- [31] J. Thomas and D. A. Imel, Recombination of electron-ion pairs in liquid argon and liquid xenon, Phys. Rev. A **36**, 614 (1987).
- [32] E. Segreto, Properties of Charge Recombination in Liquid Argon, (2024), arXiv:2405.00905 [hep-ex].
- [33] C. Adams *et al.* (MicroBooNE), Ionization electron signal processing in single phase LArTPCs. Part I. Algorithm Description and quantitative evaluation with MicroBooNE simulation, JINST **13** (07), P07006, arXiv:1802.08709 [physics.ins-det].
- [34] S. Agostinelli *et al.* (GEANT4), GEANT4—a simulation toolkit, Nucl. Instrum. Meth. A **506**, 250 (2003).
- [35] R. Acciarri *et al.* (MicroBooNE), Noise Characterization and Filtering in the MicroBooNE Liquid Argon TPC, JINST **12** (08), P08003, arXiv:1705.07341 [physics.ins-det].
- [36] B. Abi *et al.* (DUNE), First results on ProtoDUNE-SP liquid argon time projection chamber performance from a beam test at the CERN Neutrino Platform, JINST **15** (12), P12004, arXiv:2007.06722 [physics.ins-det].
- [37] W. Castiglioni, W. Foreman, I. Lepetic, B. R. Littlejohn, M. Malaker, and A. Mastbaum, Benefits of MeV-scale reconstruction capabilities in large liquid argon time projection chambers, Phys. Rev. D **102**, 092010 (2020), arXiv:2006.14675 [physics.ins-det].
- [38] A. Friedland and S. W. Li, Understanding the energy resolution of liquid argon neutrino detectors, Phys. Rev. D **99**, 036009 (2019), arXiv:1811.06159 [hep-ph].
- [39] M. A. Hernandez-Morquecho *et al.* (LArIAT), Measurements of Pion and Muon Nuclear Capture at Rest on Argon in the LArIAT Experiment, (2024), arXiv:2408.05133 [hep-ex].
- [40] C. Andreopoulos *et al.*, The GENIE Neutrino Monte Carlo Generator, Nucl. Instrum. Meth. A **614**, 87 (2010), arXiv:0905.2517 [hep-ph].
- [41] C. McGrew *et al.*, edep-sim: An Energy Deposition Simulation.
- [42] R. Wigmans, New developments in calorimetric particle detection, Prog. Part. Nucl. Phys. **103**, 109 (2018), arXiv:1807.03853 [physics.ins-det].
- [43] U. Behrens *et al.* (ZEUS Calorimeter Group), Test of the ZEUS Forward Calorimeter Prototype, Nucl. Instrum. Meth. A **289**, 115 (1990).
- [44] D. Acosta *et al.*, Electron, pion and multiparticle detection with a lead / scintillating - fiber calorimeter, Nucl. Instrum. Meth. A **308**, 481 (1991).

- [45] V. De Romeri, E. Fernandez-Martinez, and M. Sorel, Neutrino oscillations at DUNE with improved energy reconstruction, *JHEP* **09**, 030, arXiv:1607.00293 [hep-ph].
- [46] P. Abratenko *et al.* (MicroBooNE), Improving neutrino energy estimation of charged-current interaction events with recurrent neural networks in MicroBooNE, (2024), arXiv:2406.10123 [hep-ex].
- [47] J. Kopp, P. Machado, M. MacMahon, and I. Martinez-Soler, Improving Neutrino Energy Reconstruction with Machine Learning, (2024), arXiv:2405.15867 [hep-ph].
- [48] B. Abi *et al.* (DUNE), Experiment Simulation Configurations Approximating DUNE TDR, (2021), arXiv:2103.04797 [hep-ex].
- [49] A. Abed Abud *et al.* (DUNE), Doping Liquid Argon with Xenon in ProtoDUNE Single-Phase: Effects on Scintillation Light, (2024), arXiv:2402.01568 [physics.ins-det].
- [50] M. Szydagis, N. Barry, K. Kazkaz, J. Mock, D. Stolp, M. Sweany, M. Tripathi, S. Uvarov, N. Walsh, and M. Woods, NEST: A Comprehensive Model for Scintillation Yield in Liquid Xenon, *JINST* **6**, P10002, arXiv:1106.1613 [physics.ins-det].
- [51] F. Marinho, L. Paulucci, D. Totani, and F. Cavanna, LArQL: a phenomenological model for treating light and charge generation in liquid argon, *JINST* **17** (07), C07009, arXiv:2202.08905 [physics.ins-det].
- [52] A. Hitachi, T. Doke, and A. Mozumder, Luminescence quenching in liquid argon under charged-particle impact: Relative scintillation yield at different linear energy transfers, *Phys. Rev. B* **46**, 11463 (1992).
- [53] R. Acciarri *et al.* (WArP), Effects of Nitrogen contamination in liquid Argon, *JINST* **5**, P06003, arXiv:0804.1217 [nucl-ex].
- [54] Y. Li, C. Bromberg, M. Diwan, S. Kettell, S. Martynenko, X. Qian, V. Paolone, J. Stewart, C. Thorn, and C. Zhang, Parameterization of electron attachment rate constants for impurities in LArTPC detectors, *JINST* **17** (11), T11007, arXiv:2205.06888 [physics.ins-det].
- [55] N. Akchurin, K. Carrell, J. Hauptman, H. Kim, H. P. Paar, A. Penzo, R. Thomas, and R. Wigmans, Hadron and jet detection with a dual-readout calorimeter, *Nucl. Instrum. Meth. A* **537**, 537 (2005).
- [56] S. Lee *et al.*, Hadron detection with a dual-readout fiber calorimeter, *Nucl. Instrum. Meth. A* **866**, 76 (2017), arXiv:1703.09120 [physics.ins-det].
- [57] P. Abratenko *et al.* (MicroBooNE), Neutrino Event Selection in the MicroBooNE Liquid Argon Time Projection Chamber using Wire-Cell 3-D Imaging, Clustering and Charge-Light Matching, *JINST* **16** (06), P06043, arXiv:2011.01375 [physics.ins-det].
- [58] R. Acciarri *et al.* (MicroBooNE), The Pandora multi-algorithm approach to automated pattern recognition of cosmic-ray muon and neutrino events in the MicroBooNE detector, *Eur. Phys. J. C* **78**, 82 (2018), arXiv:1708.03135 [hep-ex].
- [59] R. Acciarri *et al.* (MicroBooNE), Convolutional Neural Networks Applied to Neutrino Events in a Liquid Argon Time Projection Chamber, *JINST* **12** (03), P03011, arXiv:1611.05531 [physics.ins-det].
- [60] P. Abratenko *et al.* (MicroBooNE), Semantic Segmentation with Sparse Convolutional Neural Network for Event Reconstruction in MicroBooNE, *Phys. Rev. D* **103**, 052012 (2021), arXiv:2012.08513 [physics.ins-det].
- [61] A. Abed Abud *et al.* (DUNE), Separation of track- and shower-like energy deposits in ProtoDUNE-SP using a convolutional neural network, *Eur. Phys. J. C* **82**, 903 (2022), arXiv:2203.17053 [physics.ins-det].